Reduction of the threading dislocation density in GaSb layers grown on Si(001) by molecular beam epitaxy

A Gilbert, K Graser, M Ramonda, A Trampert, J.-B Rodriguez, E Tournié

Reduction of the threading dislocation density in GaSb layers grown on Si(001) by molecular beam epitaxy

A. Gilbert[1], K. Graser[2], M. Ramonda[3], A. Trampert[2], J.-B. Rodriguez[1], E. Tournié[1,4]

[1] IES, University of Montpellier, CNRS, F- 34000 Montpellier, France
[2] Paul-Drude-Institut für Festkörperphysik, Leibniz-Institut im Forschungsverbund Berlin e.V., D- 10117 Berlin, Germany
[3] CTM, University of Montpellier, F- 34000 Montpellier, France
[4] Institut Universitaire de France (IUF), F-75005 Paris, France

Abstract: The monolithic integration of III-V semiconductors on Si emerges as a promising approach for realizing photonic integrated circuits. However, the performance and reliability of epitaxially grown devices on Si are hampered by the threading dislocation density (TDD) generated during the growth. In this study, we evaluated the efficiency of a structure, combining III-Sb-based insertion layers and thermal annealing, on the reduction of the emerging TDD in GaSb buffer layers grown on Si(001) substrates by molecular beam epitaxy. We extensively explored the impact of the thickness, composition and number of the insertion layers. Then a detailed study of the annealing cycles with different conditions was conducted. We ultimately demonstrate a record TDD in the low 10^7 cm^{-2} for a 2.25 µm GaSb buffer grown on Si(001).

I. Introduction

To surpass the limitations of current electronic devices and keep improving performances, the integration of III-V semiconductors on Silicon has emerged as a solution to develop photonic integrated circuits (PICs)[1–5]. Mastering the optical coupling between a Silicon-based photonic circuit and a III-V laser is of great interest in producing high-volume and low-cost PICs. Among III-V semiconductors, III-Sb materials and their alloys offer unrivalled opportunities for engineering Mid-IR devices due to their bandgap range spanning from 0.1 eV to 1.8 eV, their unique band structure alignments, small electron effective mass, and high carrier mobilities[6–8]. Heterogeneous integration is nowadays the most used and mature technology to combine III-Vs with Si[9–13]. However, monolithic integration, or direct epitaxy, appears as a promising scheme to offer straightforward, large-scale and low-cost integration[14]. Unfortunately, this approach is challenging, as a high density of crystal defects is created during the growth because of a polarity difference[15], and lattice parameter[16] and thermal expansion coefficient mismatches[17].

The polar on non-polar growth is responsible for forming antiphase boundaries (APBs)[15]. APBs were for long the most problematic defect, as they form electrically charged paths inside the materials and create shortcuts that kill devices[18–20]. We previously explained and demonstrated how to bury APBs in GaSb buffer layers as thin as 500 nm on Si(001) substrates[21–24]. By using the adequate

substrate surface preparation and III-V growth conditions we also succeeded to eliminate micro-twins formation[24]. The next challenge comes from the large lattice mismatch of 12% between the Si substrate and the GaSb layers. In this case, the strain is immediately relaxed by the formation of periodic arrays of misfit dislocations at the interface between the III-V and the substrate. Threading dislocations are considered to originate from imperfections in the misfit arrays[25,26] and propagate into the active region where they act as non-radiative recombination centers that degrade device performances[27–32]. As a result, several techniques for reducing the threading dislocation density (TDD) in buffer layers have been studied over the years such as thermal cycling annealing (TCAs)[33–35], strained layer superlattices (SLS) or dislocation filtering layers (DFLs)[36–38,38,39]. Thermal strain is expected to provide energy for dislocations to move and react[40], as two dislocations with opposite Burgers vectors can annihilate each other. Recently, studies on III-Sb[41,42] showed that a single thick layer provides greater TDD reduction than SLS. For instance, in GaSb systems, Yeon *et al.* [41] compared two 3 µm-thick structures. A TDD of 4×10^8 cm^{-2} was observed in a sample with five periods of 25 nm AlSb/25 nm GaSb layers, while a lower value of 9.8×10^7 cm^{-2} was achieved with a single 250 nm AlSb layer. These observations are consistent with those made on GaAs[35,39], where thick insertion layers were associated with better reduction of the TDD compared to SLS. Single AlSb insertion layers were also tested and associated to a reduction of the TDD in the subsequent growth of GaSb buffers by Mansoori *et al.*[37,42]. Their transmission electron microscopy analysis of dislocation propagation confirmed the AlSb layer's effect on threading dislocations, and two misfit dislocation networks were formed at the upper and lower interfaces of the intermediate layer[42].

In this paper, we focus on the TDD reduction in GaSb buffer layer grown on Si(001) by combining an Al(In-As)Sb-based insertion layer and high-temperature annealing. The choice of an AlSb-based interlayer to provide lateral stress is justified by its ability to withstand high temperatures and its low lattice mismatch with GaSb. We go well beyond the literature by investigating the impact of the thickness and composition modification of the insertion layer on the TDD. Then, we discuss our strategy for determining the best annealing conditions, wherein we varied the growth parameters such as the number, duration, and temperature amplitude of the cycles. Such detailed studies were never conducted before this work and enabled us to identify the key parameters that most impact the TDD.

II. Methods

All the samples were grown by solid-source molecular beam epitaxy in a RIBER COMPACT 21 system equipped with valved cracker cells for group-V elements. On-axis Si(001) substrates with a residual miscut around 0.5° were used for this study, and their surface was thermally prepared *in situ*, in a dedicated chamber, to remove the surface oxide. The typical structure consists of a 1 µm GaSb/AlSb-based/450 nm GaSb layer stack (**Fig. 1**). The GaSb and AlSb-based materials were grown at 550°C

(thermocouple reading) with a Ga growth rate of 0.3 MLs^{-1}, an Al growth rate of 0.6 MLs^{-1}, and a V/III growth-rate ratio of 2 for all samples. Heating and cooling cycles were performed right after the growth of the insertion layer, to induce thermal stress in the structure, which provides a greater probability for TDs to interact and cancel, promoting their density reduction[40]. A set of five samples was studied to identify the maximum annealing temperature before damaging the sample. We increased the temperatures from 710°C to 800°C (thermocouple), and observed that sample deterioration starts at 770°C, with the surface melting at 800°C. Consequently, we chose a conservative temperature of 750°C to perform our TCAs. We used 3 cycles to promote the maximum lateral motion of dislocation while keeping a reasonable TCAs duration.

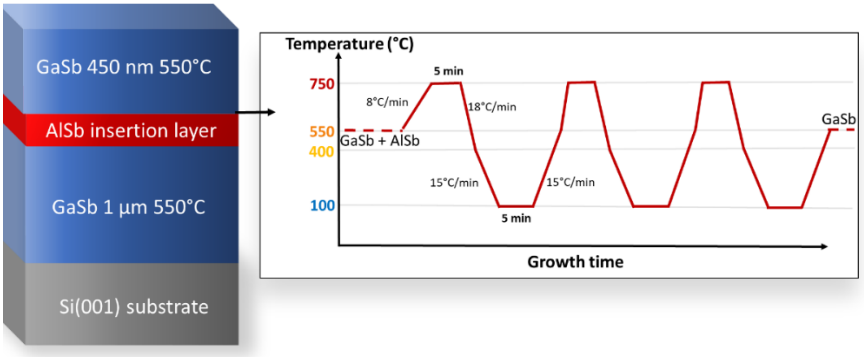

Figure 1: Schematic illustration of the typical sample's structure with its TCAs and temperature ramps description.

Atomic force microscopy (AFM) images were performed in tapping mode, using a Brucker AFM dimension 3100, to visualize the surface morphology of the samples. Each sample was mapped at room temperature for different image sizes (20 × 20, and 5 × 5 μm^2). Then, we used Electron Channeling Contrast Imaging (ECCI) in a JEOL JSM-IT800 scanning electron microscope (SEM) to estimate threading dislocation densities at the surface. The microscope is equipped with a standard annular pole-piece mounted backscatter electron (BSE) detector. For each sample, at least five ECCI images of 6.40 × 4.80 μm^2 were captured at the surface of the GaSb cap, and the mean TDD was then evaluated. In each image, some features could not be definitively identified as dislocations, despite the high quality of the micrographs. In 6.40 × 4.80 μm^2 images, we observed 7 to 278 very distinct TDs, but some features (typically 1 to 20 depending on the sample and image) could not be unambiguously identified as dislocations. The corresponding uncertainty was estimated as the average number of these features over the entire set of images for a given sample and was consistently found to be close to 10%. Finally, we used (scanning) transmission electron microscopy (S-TEM) to image the interfacial misfit dislocation networks formed at the interfaces of the insertion layers. The plan-view micrographs of the specimens were imaged in a JEOL 2100F field-emission electron microscope. The conventional

TEM sample preparation involving mechanical thinning, milling and Ar-ion polishing steps allow to select the interfacial network to observe.

III. Results and discussion

III.1. Impact of insertion layer thickness on TDD

We investigated the effect of the insertion layer thickness on the TDD using a set of seven samples, while keeping the GaSb buffer thickness constant at 1 µm and the cap thickness at 450 nm. Samples with AlSb layer thicknesses ranging from 50 to 300 nm were studied, and underwent the annealing process depicted **Figure 1** (3 cycles between 750 and 100°C). The resulting dislocation densities, measured with ECCI, are displayed in black in **Figure 2.a**. A reference sample consisting in a 1.6 µm GaSb layer without any AlSb insertion layer or TCAs is also depicted with a TDD around 4×10^8 cm^{-2} (empty circle **Fig. 2.a**). A significant improvement is seen up to an AlSb thickness of 150 nm (7.7×10^7 cm^{-2}), enabling a TDD reduction by more than a factor 5 compared to the reference sample. However, for AlSb thicknesses greater than these values, only a marginal improvement is observed.

Plan-view STEM images of the 50, 150 and 300 nm insertion layers were performed to analyze the lower misfit dislocation networks, as increasing the AlSb thickness should affect this interface most. **Figure 2.b** taken from the sample with a 50 nm AlSb layer shows a complex disorganized dislocation network dominated by MDs propagating along the perpendicular [110] and [$1\bar{1}0$] directions. The comparison with the thicker samples (**Fig. 2.c and 2.d**) indicates that the overall arrangement of the MDs becomes denser and more regular when the AlSb thickness increases. Thanks to the STEM images it is possible to estimate the plastic relaxation and the residual strain in the AlSb layer. Based on the **g·b** invisibility criterion of the samples, the zoom in the STEM images of **Figure 2** demonstrates the presence of pure-edge 90°-type MDs grouping in rectangular patterns. The plastic strain relieved in the AlSb layer can be calculated by measuring the average distance between MDs in these rectangular areas $d_{MDs<110>}$ in the <110> directions[43]:

$$\varepsilon_p = |\overrightarrow{b_\parallel}| \cdot \frac{1}{d_{MDs<110>}}$$

With $\overrightarrow{b_\parallel} = \frac{a}{\sqrt{2}}$ = 0.43 nm, the effective Burgers vector parallel to the (001) interface plane.

The average distances between the dislocations of 144 nm, 104 nm, and 88 nm (± 10 nm) have respectively been found for the 50, 150 and 300 nm-thick AlSb samples, based on at least 5 TEM images per sample. As a result, the AlSb plastic relaxation is about 0.29%, 0.41% and 0.49% in the samples. With a lattice mismatch of 0.65% between GaSb and AlSb at room temperature, this means that the insertion layer still has a residual strain of about 0.36%, 0.24% and 0.16%, respectively, as displayed in

red in **Figure 2.a**. **Figure 2** clearly shows that the TDD reduction is related to the decrease of the AlSb residual strain. The strain in the AlSb layer is indeed relieved by the formation of a MD array at the interface with GaSb (see **Figure 2. b, c and d**), which is formed by the strain-induced glide of the threading arms. This strain relaxation process implies the movement of a large number of TDs, which greatly increases the probability of interaction and annihilation, resulting in the observed decrease in TDD. This explains the need for a layer with a thickness much larger than the critical thickness, which was already suggested in references [37,41,42]. However, as the residual strain becomes relatively low, the process becomes less efficient. Accordingly, **Figure 2** shows a saturation of the TDD at a thickness of 100 – 150 nm, despite a residual strain of 0.24%, which could be attributed to the very high density of the MD array at this stage, preventing further TD glide.

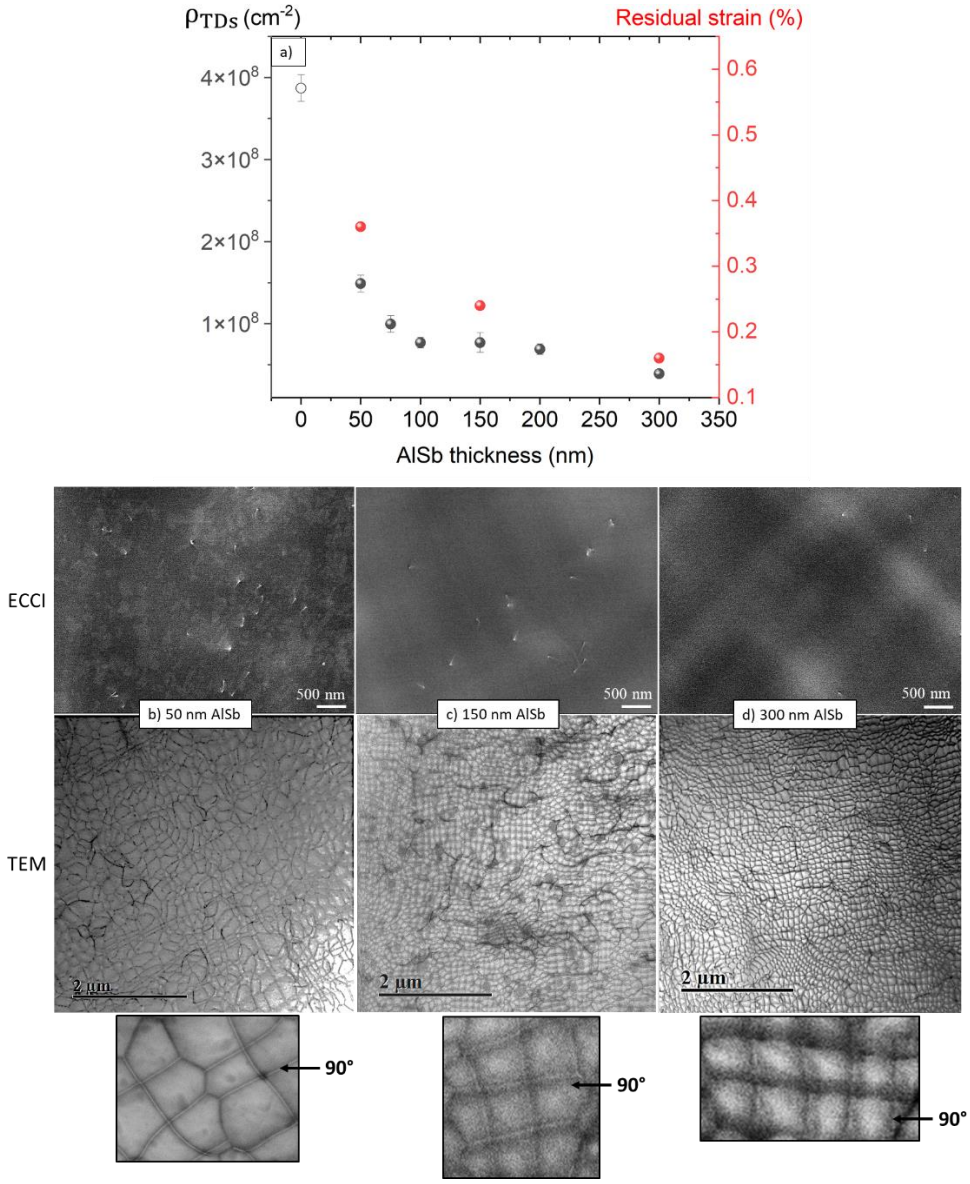

Figure 2: a) Evolution of the TDD (black) and residual strain (red) with the AlSb layer thicknesses. The 1.6 µm GaSb reference sample is represented by an empty circle. Representative ECCI and plan-view

STEM images of the misfit dislocation network of the GaSb/AlSb lower interface for AlSb layers of b) 50 nm, c) 150 nm, c) 300 nm are displayed. The enlargements highlight the rectangular areas formed by the 90° misfit dislocations, that become more regular with the increasing thickness.

III.2. Impact of insertion layer composition on TDD

We then varied the composition of the insertion layer to change the mismatch sign/magnitude introduced in the system. All samples underwent the same annealing process as before, consisting of 3 TCAs involving heating at 750°C, a 5 minutes-hold at this temperature, followed by cooling down to 100°C for 5 minutes (**Fig. 1**). A tensile strain (negative mismatch) is introduced when AlAsSb layers with an As composition larger than 8.5% is used, whereas a compressive strain (positive mismatch) is obtained for lower As contents or with AlInSb layers, as indicated in **Table 1**. Four AlAsSb insertion layers with arsenic contents ranging from 5.5 to 21.5%, and two AlInSb insertion layers with indium content of 1 and 6% were investigated. All insertion layers were 150 nm-thick and covered by 450 nm GaSb cap layers.

Table 1: Mismatch values calculated for each insertion layer and root mean square (RMS) roughness extracted from the AFM images **Figure 3** with the Gwyddion software[44].

Layer	$AlAs_{0.215}Sb$	$AlAs_{0.14}Sb$	$AlAs_{0.085}Sb$	$AlAs_{0.055}Sb$	AlSb	$AlIn_{0.01}Sb$	$AlIn_{0.06}Sb$
Mismatch (%)	-1	-0.45	0	0.22	0.65	0.71	0.99
RMS (nm)	3.80	1.47	1.03	1.26	1.12	1.39	1.34

The TDDs measured using ECCI are plotted in **Figure 3.a** and show that tensile strain (negative values) is less efficient than compressive strain for the density reduction. The lattice-matched insertion layer depicted in black (**Fig. 3.a**) has the highest TDD of 8×10^8 cm^{-2}, which demonstrates the major impact of the mismatch to promote dislocation glide and TDD reduction. On the contrary, the TDD decreases when the compressive strain (positive values) increases. Low TDDs in the $6 - 7 \times 10^7$ cm^{-2} are achieved for the AlInSb compressive layers. However, considering the error bars these values are similar to that of the AlSb layer (7.7×10^7 cm^{-2}), which is easier to grow.

The associated 5×5 µm² AFM images of these samples are shown in **Figure 3.b.** The surfaces demonstrate similar features with steps resulting from a step-flow growth mode and many dislocations appearing as dark pits, except for the sample with the $AlAs_{0.215}Sb$ insertion layer (mismatch of -1%). The higher As content may induce the line defects observed at the AFM surface. A light crosshatch appears in the samples with no or low positive mismatches and the pattern is more pronounced in the

[1$\bar{1}$0] direction. With higher positive mismatches, the more discernible cross-hatch pattern indicates that a higher density of dislocation glide and form MDs segments at the interface.

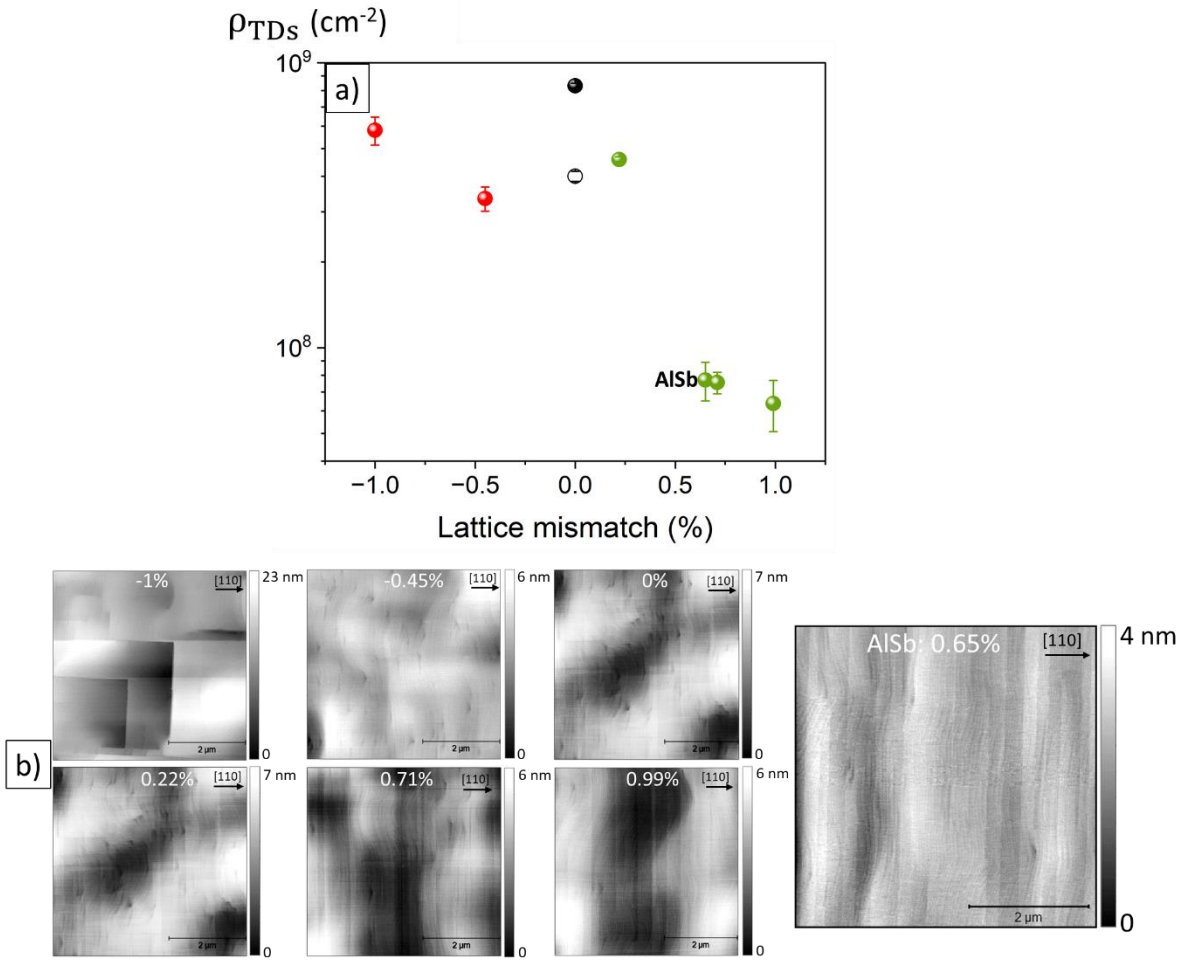

Figure 3: a) Evolution of the TDD as a function of the insertion layer lattice mismatch with tensile strain indicated in red and compressive strain in green. The lattice matched insertion layer is indicated in black and the 1.6 µm GaSb reference sample is represented by an empty circle. b) 5×5 µm² AFM images of the surface of the samples with their associated lattice mismatch. The structure with the AlSb insertion layer is highlighted at the right.

III.3. Impact of thermal cyclic annealing (TCAs) on TDD

High-temperature annealing is expected to promote more energy to the system to favor dislocation motions and thus increase the interaction probability for annihilation[45]. In this set of experiments, we maintained an identical stacking of 1 µm GaSb buffer followed by a 150 nm AlSb layer, and a 450 nm GaSb cap, all grown at 550°C. The number of cycles, the hold time of the steps at high and low temperatures, and the temperature amplitude impact on the TDD are investigated. **Figure 4** shows the TDD measured on top of the GaSb cap after the different TCAs processes. We systematically compared these samples with a no TCA reference sample having a TDD of 5.8×10^7 cm^{-2} (empty circle in **Fig. 4**)

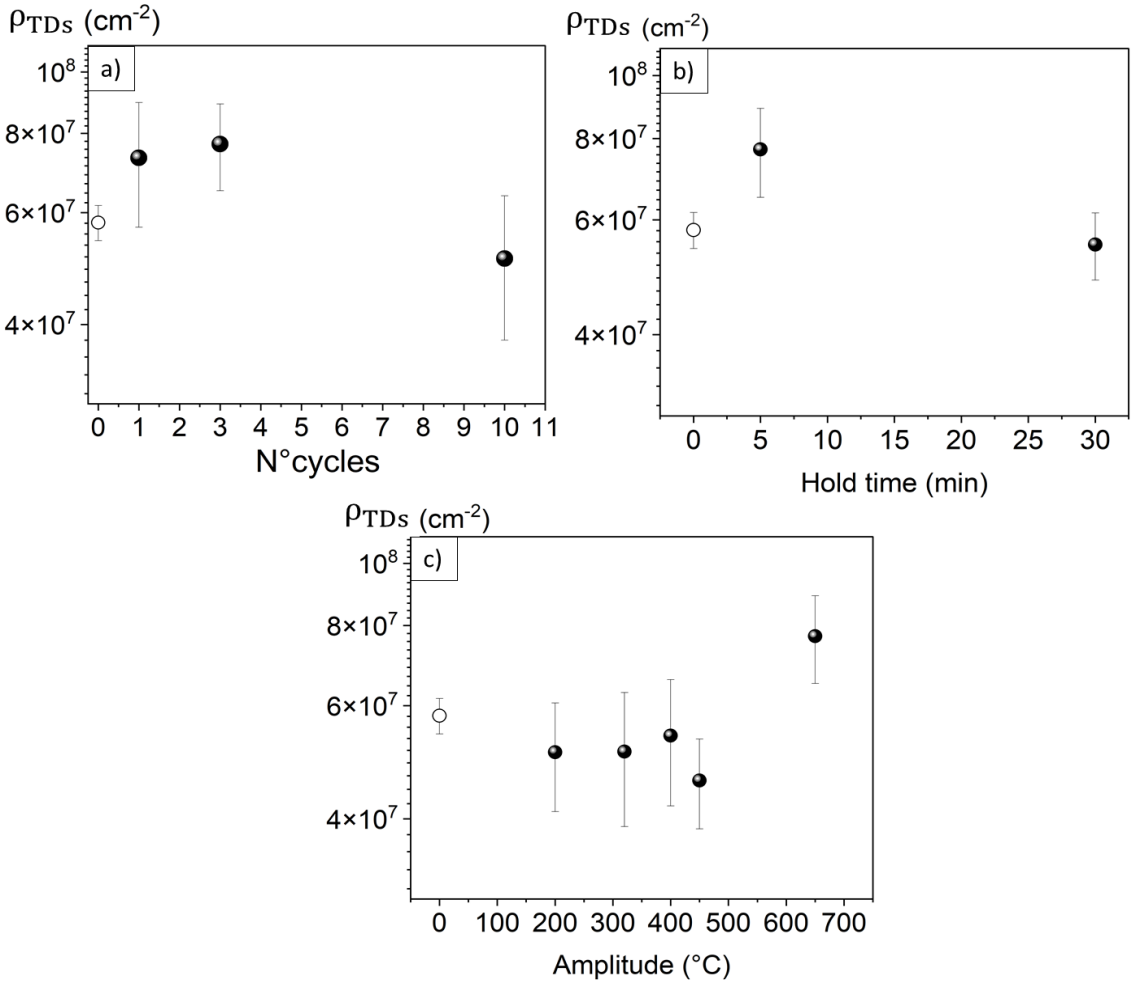

Figure 4: a) Evolution of the TDD with the number of cycles b) with the hold time at high and low temperatures and c) with the temperature amplitude. The sample without any annealing is represented by empty circles.

Figure 4 shows that the TDD is very little impacted by the annealing steps for a wide range of TCA conditions. Notably, the residual TDD is always very similar to the value obtained without any annealing. However, it is important to note that even without the additional annealing steps, thermal energy is transferred to dislocations during the growth of the top GaSb layer. Although its growth temperature (550°C) is relatively modest compared to the maximum annealing temperature used in our study (750°C), the energy transferred during the process may be large enough to allow efficient dislocation movement, which is supported by our observation of a dense network of MD arms even in the absence of any additional annealing step.

III.4. Impact of the number of AlSb layers on TDD

The previous sections demonstrated that thermal annealing is ineffective in reducing the TDD, which saturates in the $\sim 6 \times 10^7 \text{cm}^{-2}$ range for an AlSb insertion layer of 100-150 nm and that AlSb is the most efficient and convenient material. The saturation of the TDD reduction might originate from the

density of the MDs networks formed at the interfaces of the 150 nm AlSb layer. As the MD density increases, the compact array formed may hinder the glide necessary for further TDs annihilation. In this context, the growth of a second AlSb covered by an additional GaSb layer should then help to overcome this saturation by forming fresh AlSb/GaSb interfaces. We then grew a sample with two AlSb layers; the first one of 150 nm and the second one of 300 nm, separated by a 350 nm GaSb layer (**Fig. 5**). The second layer of AlSb needs to be thicker to compensate for the initially lower TDD and to ensure a high probability of annihilation.

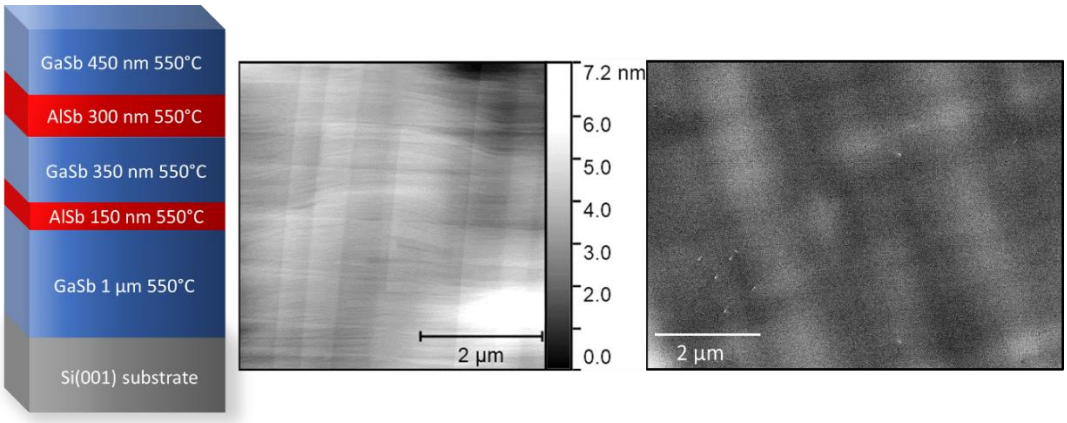

Figure 5: AFM and ECCI images of the double AlSb structure.

The AFM image demonstrates a morphology resulting from a step-flow growth mode, and a crosshatched surface with a low roughness of 1.32 nm (**Fig. 5**). Our statistical analysis of the ECCI images reveals a TDD reduction down to $1.69 \pm 0.19 \times 10^{7}$ cm^{-2} for a total structure thickness of 2.25 µm. This represents more than a factor of 3 improvement compared to the result with a single AlSb layer (**Fig. 6**), and a significant achievement compared to what is observed in the literature. Similar densities to those of our single AlSb layer are reported with buffers that are two to three times thicker than our sample (1.6 µm). Moreover, our result with the two AlSb layers is the best to date in the GaSb system (**Fig. 6**).

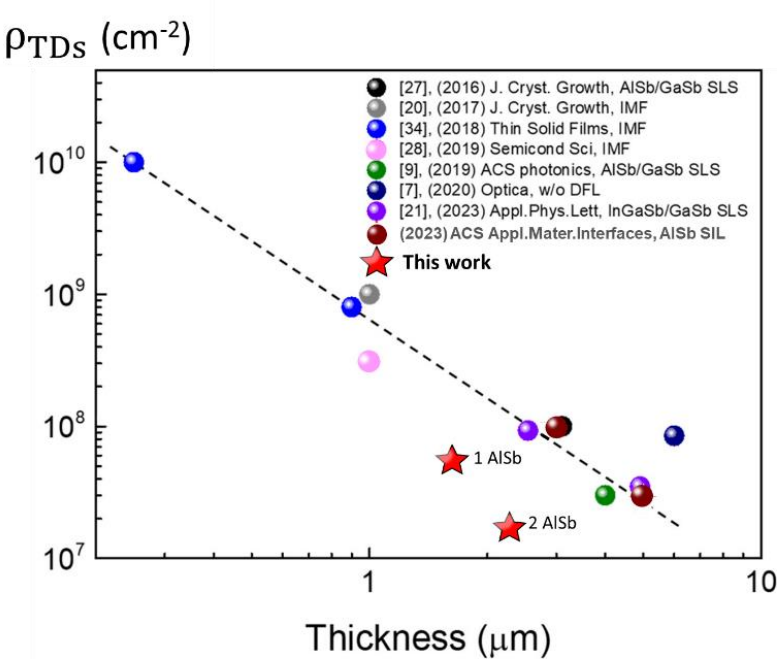

Figure 6: Threading dislocation densities of GaSb/Si layers as a function of the structure thickness reported by other groups and comparison with our results obtained with 1 AlSb and 2 AlSb insertion layers (stars). Adapted from Yeon *et al.*[41].

IV. Conclusion

The high density of treading dislocations is the main technological issue faced at the moment by the whole community interested in the epitaxy of III-V lasers on Si-photonic platforms. In this work, we have extensively investigated the impact of III-As,Sb-based insertion layers and thermal cycle annealing in the case of GaSb/Si heteroepitaxy. AlSb appeared as the most efficient material to decrease the TDD. The insertion of a 150 nm AlSb layer led to a TDD reduction in the $\sim 6 \times 10^7$ cm^{-2} for a structure thickness of 1.6 µm. Increasing the thickness of the insertion layer did not further reduce the TDD significantly. This saturation effect with the thickness might be due to the close-packed misfit dislocations geometry already achieved in the interfacial MDs networks of the 150 nm AlSb, which prevents further dislocation motion and annihilation.

Additionally, our complete study of TCAs showed that the TDD was not affected by the additional thermal energy provided by high temperature annealing. It is believed that the energy transferred to the TDs during the growth of the GaSb cap layer at 550°C would be large enough to promote TDs glide in our III-Sb materials, and to ensure that most of the dislocation interactions have occurred. In this context, TCAs do not contribute significantly to further dislocation movement. This behaviour contrasts with observations in GaAs materials, where TCAs do impact the TDD[33,46–48]. In fact, the growth temperature of GaAs (550-650°C) is well below its melting point of 1238°C, which limits the

dislocation glide and climb process during epitaxy, and makes the post-growth annealing very effective in this case. In contrast, the GaSb growth temperature of 550°C is relatively close to its melting point of 712°C, and this temperature is probably high enough to promote the movement of the TDs and thus their interactions. Still, we note that the combination of insertion layers and TCAs in GaAs/Si results in TDD in on the order of 10^6 cm^{-2} [33,35,46–51], which is lower than our result despite careful optimization of the annealing step. The higher TDD values obtained in the case of the growth of GaSb on Si could be due to more fundamental structural properties differences between GaSb and GaAs such as the lattice parameters (and thus {111} plane spacing), the covalent bond strengths, or the density of point defects (vacancies and interstitials), many factors, that could impact the effectiveness of the strain relaxation process on the TDD reduction. While these phenomena are complex and challenging to study - and beyond the scope of this paper - they motivate further investigation in the future.

Finally, we investigated a solution to overcome this bottleneck by adding a second layer with compressive strain. This promotes the formation of new, complex misfit networks, allowing for further dislocation glide and annihilation. Indeed, the insertion of another AlSb layer in the buffer resulted in a TDD reduction down to $\sim 1.7 \times 10^7 \text{cm}^{-2}$, the best ever value reported in the literature.

Acknowledgments

Part of this work was supported by the France 2030 program (Equipex EXTRA, ANR11-EQPX-0016, Equipex+ HYBAT, ANR-21-ESRE-0026), the ANR-DFG FILTER project (ANR-20-CE92-0045), the ANR PIANIST (ANR-21-CE09-0020) and NUAGES (ANR-21-CE24-0006) projects, and the French Renatech network. We acknowledge the financial support provided by the European COST Action OPERA (CA-20116) through the short-term scientific mission program.

Bibliography

[1] P. S. Peercy, *Nature* **2000**, *406*, 1023.
[2] K. Kitayama, M. Notomi, M. Naruse, K. Inoue, S. Kawakami, A. Uchida, *APL Photonics* **2019**, *4*, 090901.
[3] S. Y. Siew, B. Li, F. Gao, H. Y. Zheng, W. Zhang, P. Guo, S. W. Xie, A. Song, B. Dong, L. W. Luo, C. Li, X. Luo, G.-Q. Lo, *J. Light. Technol.* **2021**, *39*, 4374.
[4] D. A. B. Miller, *Nat. Photonics* **2017**, *11*, 403.
[5] M. Lipson, *Nat. Mater.* **2022**, *21*, 974.
[6] I. Vurgaftman, J. R. Meyer, L. R. Ram-Mohan, *J. Appl. Phys.* **2001**, *89*, 5815.
[7] J.-W. Luo, A. Franceschetti, A. Zunger, *Nano Lett.* **2008**, *8*, 3174.
[8] E. Tournié, L. Cerutti, *Mid-Infrared Optoelectronics*, Woodhead Publishing, **2019,** First Edition, Ch. 1, pp. 4-6.
[9] D. Liang, J. E. Bowers, *Nat. Photonics* **2010**, *4*, 511.
[10] N. Zia, H. Tuorila, J. Viheriälä, S.-P. Ojanen, E. Koivusalo, J. Hilska, M. Guina, *Opt. Express* **2022**, *30*, 24995.
[11] T. Aihara, T. Hiraki, T. Fujii, K. Takeda, T. Tsuchizawa, T. Kakitsuka, H. Fukuda, S. Matsuo, *Opt. Express* **2022**, *30*, 15820.
[12] G. Roelkens, J. Zhang, L. Bogaert, M. Billet, D. Wang, B. Pan, C. Krückel, E. Soltanian, D. Maes, T. Vanackere, T. Vandekerckhove, S. Cuyvers, J. De Witte, I. Luntadila Lufungula, X. Guo, H. Li, S. Qin, G. Muliuk, S. Uvin, B. Haq, C. Op de Beeck, J. Goyvaerts, G. Lepage, P. Verheyen, J. Van

Campenhout, G. Morthier, B. Kuyken, D. Van Thourhout, R. Baets, *IEEE J. Sel. Top. QUANTUM Electron.* **2023**, *29*, DOI: 10.1109/JSTQE.2022.3222686.
[13] G. Roelkens, J. Zhang, L. Bogaert, E. Soltanian, M. Billet, A. Uzun, B. Pan, Y. Liu, E. Delli, D. Wang, V. B. Oliva, L. T. Ngoc Tran, X. Guo, H. Li, S. Qin, K. Akritidis, Y. Chen, Y. Xue, M. Niels, D. Maes, M. Kiewiet, T. Reep, T. Vanackere, T. Vandekerckhove, I. L. Lufungula, J. De Witte, L. Reis, S. Poelman, Y. Tan, H. Deng, W. Bogaerts, G. Morthier, D. Van Thourhout, B. Kuyken, *APL Photonics* **2024**, *9*, 010901.
[14] M. Tang, J. S. Park, Z. Wang, S. Chen, P. Jurczak, A. Seeds, H. Liu, *Prog. Quantum Electron.* **2019**, *66*, 1.
[15] H. Kroemer, *Journal of Crystal Growth* **1987**, *81*, 193.
[16] J. W. Matthews, A. E. Blakeslee, *J. Cryst. Growth* **1974**, *27*, 118.
[17] V. K. Yang, M. Groenert, C. W. Leitz, A. J. Pitera, M. T. Currie, E. A. Fitzgerald, *J. Appl. Phys.* **2003**, *93*, 3859.
[18] H. Kroemer, K. J. Polasko, S. C. Wright, *Appl. Phys. Lett.* **1980**, *36*, 763.
[19] P. N. Uppal, H. Kroemer, *J. Appl. Phys.* **1985**, *58*, 2195.
[20] K. Li, J. Yang, Y. Lu, M. Tang, P. Jurczak, Z. Liu, X. Yu, J. Park, H. Deng, H. Jia, M. Dang, A. M. Sanchez, R. Beanland, W. Li, X. Han, J. Zhang, H. Wang, F. Liu, S. Chen, A. Seeds, P. Smowton, H. Liu, *Adv. Opt. Mater.* **2020**, *8*, 2000970.
[21] I. Lucci, S. Charbonnier, L. Pedesseau, M. Vallet, L. Cerutti, J.-B. Rodriguez, E. Tournié, R. Bernard, A. Létoublon, N. Bertru, A. Le Corre, S. Rennesson, F. Semond, G. Patriarche, L. Largeau, P. Turban, A. Ponchet, C. Cornet, *Phys. Rev. Mater.* **2018**, *2*, 060401.
[22] C. Cornet, S. Charbonnier, I. Lucci, L. Chen, A. Létoublon, A. Alvarez, K. Tavernier, T. Rohel, R. Bernard, J.-B. Rodriguez, L. Cerutti, E. Tournié, Y. Léger, M. Bahri, G. Patriarche, L. Largeau, A. Ponchet, P. Turban, N. Bertru, *Phys. Rev. Mater.* **2020**, *4*, 053401.
[23] M. R. Calvo, J.-B. Rodriguez, C. Cornet, L. Cerutti, M. Ramonda, A. Trampert, G. Patriarche, E. Tournié, *Adv. Electron. Mater.* **2022**, *8*, 2100777.
[24] M. Rio Calvo, Épitaxie de GaSb Sur Substrat Si(001)“on-Axis”Pour l’optoélectronique Intégrée, These de doctorat, Montpellier, **2020**.
[25] J. M. Kang, M. Nouaoura, L. Lassabatère, A. Rocher, *J. Cryst. Growth* **1994**, *143*, 115.
[26] Y. B. Bolkhovityanov, O. P. Pchelyakov, *Phys.-Uspekhi* **2008**, *51*, 437.
[27] B. Kunert, Y. Mols, M. Baryshniskova, N. Waldron, A. Schulze, R. Langer, *Semicond. Sci. Technol.* **2018**, *33*, 093002.
[28] J.-R. Reboul, L. Cerutti, J.-B. Rodriguez, P. Grech, E. Tournié, *Appl. Phys. Lett.* **2011**, *99*, 121113.
[29] A. Remis, L. Monge-Bartolomé, G. Boissier, M. Waguaf, J.-B. Rodriguez, L. Cerutti, E. Tournié, *J. Appl. Phys.* **2023**, *133*, 093103.
[30] M. Rio Calvo, L. Monge-Bartolomé, M. Bahriz, G. Boissier, L. Cerutti, J.-B. Rodriguez, E. Tournié, *Optica* **2020**, *7*, 263.
[31] L. Cerutti, J. B. Rodriguez, E. Tournie, *IEEE Photonics Technol. Lett.* **2010**, *22*, 553.
[32] J. B. Rodriguez, L. Cerutti, P. Grech, E. Tournié, *Appl. Phys. Lett.* **2009**, *94*, 061124.
[33] J. W. Lee, H. Shichijo, H. L. Tsai, R. J. Matyi, *Appl. Phys. Lett.* **1987**, *50*, 31.
[34] Y. Takano, M. Hisaka, N. Fujii, K. Suzuki, K. Kuwahara, S. Fuke, *Appl. Phys. Lett.* **1998**, *73*, 2917.
[35] C. Shang, J. Selvidge, E. Hughes, J. C. Norman, A. A. Taylor, A. C. Gossard, K. Mukherjee, J. E. Bowers, *Phys. Status Solidi A* **2021**, *218*, 2000402.
[36] J. Selvidge, J. Norman, E. T. Hughes, C. Shang, D. Jung, A. A. Taylor, M. J. Kennedy, R. Herrick, J. E. Bowers, K. Mukherjee, *Appl. Phys. Lett.* **2020**, *117*, 122101.
[37] A. Mansoori, S. J. Addamane, E. J. Renteria, D. M. Shima, M. Behzadirad, E. Vadiee, C. Honsberg, G. Balakrishnan, *Sol. Energy Mater. Sol. Cells* **2018**, *185*, 21.
[38] A. Mansoori, S. J. Addamane, E. J. Renteria, D. M. Shima, G. Balakrishnan, *J. Electron. Mater.* **2020**, *49*, 7153.
[39] M. Dang, H. Deng, S. Huo, R. R. Juluri, A. M. Sanchez, A. J. Seeds, H. Liu, M. Tang, *J. Phys. Appl. Phys.* **2023**, *56*, 405108.

[40] W. Li, S. Chen, M. Tang, J. Wu, R. Hogg, A. Seeds, H. Liu, I. Ross, *J. Appl. Phys.* **2018**, *123*, 215303.
[41] E. Yeon, S. Woo, R. J. Chu, I.-H. Lee, H. W. Jang, D. Jung, W. J. Choi, *ACS Appl. Mater. Interfaces* **2023**, *15*, 55965.
[42] S. J. Addamane, D. M. Shima, A. Mansoori, G. Balakrishnan, *J. Appl. Phys.* **2020**, *128*, 225301.
[43] D. J. Dunstan, *J. Mater. Sci. Mater. Electron.* **1997**, *8*, 337.
[44] P. Klapetek, D. Nečas, C. Anderson, **n.d.**
[45] K. Mukherjee, in *Reliab. Semicond. Lasers Optoelectron. Devices* (Eds.: R.W. Herrick, O. Ueda), Woodhead Publishing, **2021**, pp. 113–176.
[46] H. Uchida, T. Soga, H. Nishikawa, T. Jimbo, M. Umeno, *J. Cryst. Growth* **1995**, *150*, 681.
[47] M. Yamaguchi, M. Tachikawa, Y. Itoh, M. Sugo, S. Kondo, *J. Appl. Phys.* **1990**, *68*, 4518.
[48] C. lee, H. Liu, Z. Liu, J. Ye, H. Zhai, S. Liu, J. Lin, Q. Wang, Q. Wang, *Appl. Phys. A* **2023**, *130*, DOI: 10.1007/s00339-023-07162-3.
[49] H. Okamoto, Y. Watanabe, Y. Kadota, Y. Ohmachi, *Jpn. J. Appl. Phys.* **1987**, *26*, L1950.
[50] D. Jung, P. G. Callahan, B. Shin, K. Mukherjee, A. C. Gossard, J. E. Bowers, *J. Appl. Phys.* **2017**, *122*, 225703.
[51] Y.-H. Ko, K.-J. Kim, J. Baek, S. Lee, D.-J. Kim, J.-H. Kim, H. Guim, W. S. Han, *Solid-State Electron.* **2019**, *166*, 107763.